Journal of Quantitative Spectroscopy & Radiative Transfer 203 (2017) 119–132

Contents lists available at ScienceDirect

Journal of Quantitative Spectroscopy & Radiative Transfer

journal homepage: www.elsevier.com/locate/jqsrt

Measurement of positions, intensities and self-broadening line shape parameters of H_2O lines in the spectral ranges 1850–2280 cm^{-1} and 2390–4000 cm^{-1}

J. Loos *, M. Birk, G. Wagner

Remote Sensing Technology Institute, German Aerospace Center (DLR), D-82234 Wessling, Germany

ARTICLE INFO

Article history:
Received 12 January 2017
Received in revised form
15 February 2017
Accepted 24 February 2017
Available online 2 March 2017

Keywords:
Water vapor
Infrared line parameters
Line positions
Intensities
Self-broadening line shape parameters

ABSTRACT

A Bruker IFS 125 HR Fourier transform spectrometer was used to measure several pure water transmittance spectra in the spectral range 1850–4000 cm^{-1}. A total of 15 measurements with absorption path lengths between 24.9 cm and 174.6 m and sample gas pressures from 0.1 to 20 mbar were performed at 296 K. The transmittance spectra were corrected for various error sources and were analyzed in the spectral ranges 1850–2280 cm^{-1} and 2390–4000 cm^{-1} for the majority of intensities between 3×10^{-26} and 3×10^{-19} cm $molecule^{-1}$. A multispectrum fitting approach was used applying a quadratic speed-dependent Voigt model extended to account for line mixing in the Rosenkranz first order perturbation approximation. Line positions, intensities, self-broadening widths, their speed-dependence and in some cases line mixing had to be adjusted for fitting the measurements to noise level. An extensive error estimation calculation was performed propagating several instrumental and measurement errors into individual parameter inaccuracies. The determined parameters are compared to HITRAN12 and independent experimental values while intensities are compared to recent *ab initio* calculations performed at UCL. The overall agreement between *ab initio* calculations and experimental values is remarkable and below 1% in most cases. The determined line parameters are provided as a supplement to this publication.

1. Introduction

The infrared absorption spectrum of water vapor is widely studied because of its major role in atmospheric radiative and physical processes. Thus, accurate knowledge of spectral absorption parameters is essential for the investigation of Earth's atmosphere, the simulation of the atmosphere's heat balance and the monitoring and prediction of Earth's climate.

The ground based remote sensing networks NDACC [1] and TCCON [2] deliver data products widely used in the atmospheric science community e.g. in trend evaluation, satellite validation or for assessment of chemical transport models. The analysis of ground based remote sensing data relies on accurate spectroscopic reference data. This is especially important for water vapor. Due to its large column amount and strong and sometimes interfering spectrum relevant line intensities range over several orders of magnitude.

It was shown by Schneider et al. [3–6] that the use of HITRAN12 [7] data in ground based remote sensing leads to large fitting residuals and errors in water vapor profile retrieval. These errors were tracked back to insufficient knowledge of line parameters and the use of the Voigt line shape model. It was shown that updating water vapor parameters and the use of a speed-dependent Voigt line shape leads to lower residuals and better agreement of retrieved profiles to *in situ* measurements. Furthermore, inconsistencies of results retrieved from different spectral ranges were detected. Timofeyev et al. [8] report that inaccuracies of water vapor parameters are the major source for systematic errors in ground based remote sensing. Birk and Wagner [9] showed that the use of a Voigt profile in the analysis of laboratory spectra leads to systematic errors in radiative transfer calculations when extrapolating in optical depth.

This work is the first part of an extensive research activity on water vapor absorption in the spectral range 1850–4000 cm^{-1} with the aim of an experimental line parameter list according to the needs of ground based atmospheric remote sensing. Several pure water transmittance spectra were measured and analyzed using a multispectrum fitting approach applying a speed-dependent Voigt

* Corresponding author.
E-mail addresses: joep.loos@dlr.de (J. Loos), manfred.birk@dlr.de (M. Birk), georg.wagner@dlr.de (G. Wagner).

http://dx.doi.org/10.1016/j.jqsrt.2017.02.013
0022-4073/

profile extended to account for line mixing in the Rosenkranz first order perturbation approximation [10]. A line list including line positions, intensities, self-broadening parameters, self-speed-dependence and -shifts as well as some line mixing parameters is presented and compared to spectroscopic databases, experimental values and calculations.

This work is part of the corresponding author's Ph.D. thesis "Verbesserung der spektroskopischen Datenbasis von H_2O für die Anwendung in bodengebundener Fernerkundung der Atmosphäre" to be submitted at the Karlsruhe Institute of Technology.

2. Experiment

The measurements were performed using a Fourier-Transform spectrometer in combination with two absorption gas cells. The measurements are dedicated to position, intensity and self-line shape parameter retrieval of water vapor absorption lines. Apart from water spectra several pure N_2O spectra at low pressures in the Doppler regime were recorded for characterization of the instrumental line shape function (ILS).

2.1. Fourier-Transform spectrometer

A Bruker IFS 125 HR Fourier-Transform spectrometer was used for all measurements. The interferometer housing was evacuated using a turbomolecular pump and a cold trap filled with LN_2 in order to reduce residual water absorption in the spectra. As radiation source the internal thermal radiator (globar) was used. A 1 mm diameter entrance aperture was chosen. The used beam splitter consisted of CaF_2 substrate coated with silicon. The measurements were performed using either a short absorption path cell or a White-type multireflection cell. The internal InSb detector in combination with an optical short-pass filter was used for signal detection. The optical filter is necessary to reduce the photon flux onto the detector and thus increase the Signal-to-Noise ratio. In order to reduce channeling, the filter was wedged. It was located right in front of the detector's input window. The measurement parameters are summarized in Table 1.

2.2. Short absorption path cell

A double-jacket Duran-glass single pass cell with an inner diameter of 4 cm and an absorption path length of 24.9(1) cm was used for the measurements. The cell's windows are made of AgCl and are – in order to reduce channeling – wedged and mounted in a slightly tilted position. The cell was located inside the evacuated interferometer's sample compartment. The cell is designed for the temperature range 195–300 K and its temperature is controlled by flowing temperature-controlled fluid through the double jacket. The temperature is measured with two calibrated PT100 temperature sensors attached to the outer cell walls. For temperature readout and logging LakeShore 218E temperature monitor instruments were used. The combined temperature sensor and readout accuracy is 0.2 K. The cell has previously been used for several absorption studies e.g [11–14].

Table 1
Measurement parameters. MOPD denotes the maximum optical path difference.

Source	Globar
Absorption path length l (m)	0.249–174.61
Field stop diameter (mm)	1.0
Beam splitter	Si-coated CaF_2
Sample cell window material	Short cell: AgCl Multireflection cell: CaF_2
Optical filter	Low pass 4000 cm^{-1}
Detector	Internal InSb
MOPD (cm)	180 or 250 (sample gas measurements) 9 (empty cell measurements)

2.3. Multireflection cell

The applied White-type multireflection cell has a base length of 0.80 m and is directly attached to the interferometer's sample compartment. The absorption path length can be set in the range from 14.4 to 206.4 m in steps of 6.4 m with a specified absorption path accuracy of 0.1%. The beam is injected via a custom made transfer optics setup located in the interferometer's sample compartment. The cell's temperature can be controlled by flowing temperature controlled fluid through the cell's double jacket and through the mounts of the optical mirrors inside the cell. The cell temperature was measured using eight PT100 temperature sensors. Four sensors were attached to the cell's wall, two to the T-mirror and two to the D-mirrors. For temperature readout and logging LakeShore 218E temperature monitor instruments were used. The combined temperature sensor and readout accuracy is 0.10 K. The cell has been used previously in numerous measurements of molecular e.g [15–18]. and its basic setup is described in [12].

2.4. Sample preparation, setup and measurements

2.4.1. Sample preparation

As sample gas evaporated water vapor from a liquid tap water reservoir was used. In order to clean the liquid water prior to usage it was frozen and the dissolved air was pumped off several times.

2.4.2. Short cell measurements

The sample cell is located in the interferometer's sample compartment and can be filled from the outside without venting the instrument. In order to decrease the surface-volume ratio a 35 l stainless steel vessel was attached to the cell. This is necessary because of the wall-sticking nature of water molecules. The liquid water reservoir made of Duran glass had a volume of 20 ml and was about half filled. The whole system was connected to a pumping system with a LN_2 cold trap, a rotary and a turbomolecular pump. The pressure inside the system was measured using mks 627B and 127 A Baratron absolute pressure gauges with full scale ranges of 0.1, 1, 10 and 100 mbar. The gauges were controlled and their readings logged using mks PR4000B pressure readout instruments. The cell's temperature was controlled using a Julabo F10 refrigerator with specified temperature stability of ± 0.02 K. Before filling the cell and measuring water spectra, empty cell background spectra with reduced resolution were recorded. Because of water vapor absorption features present in the background spectra some high resolution background spectra were recorded as well. After finishing the background spectra, water vapor was evaporated into the cell until the desired pressure was reached. Measurements were started after the pressure inside the cell stabilized. Several consecutive measurement blocks were performed so that the stability during measurements could be checked.

2.4.3. Multireflection cell measurements

The setup for multireflection cell measurements is shown in Fig. 1. The cell is directly attached to the interferometer's sample compartment and the beam is injected via custom-built transfer optics. The whole system could be pumped with a LN_2 cold trap, a rotary pump and a turbomolecular pump. The pressure inside the cell was measured using mks 627B, 120A and 127A Baratron absolute pressure gauges with full scale ranges of 0.1, 1, 10 and

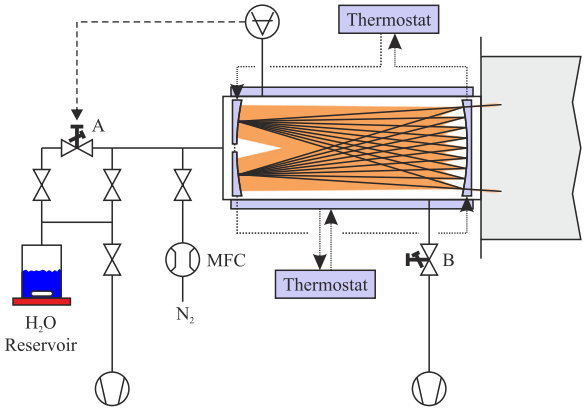

Fig. 1. Schematic setup of pure water White cell measurements. The cell is directly attached to the interferometer's sample compartment and its temperature is controlled by two refrigerators. During the measurements the pressure inside the cell is kept constant via a pressure controlled valve (A). The flow rate is set using valve (B) which was calibrated with a flow of dry nitrogen and an mks mass flow controller (MFC).

Table 2
H_2O measurement conditions. SNR_{RMS} gives the root mean square signal-to-noise ratio at 2500 cm^{-1}. f_{HDO} denotes a fitted scaling factor for HDO abundance (see Section 3).

#	p_{H2O} (mbar)	l (m)	T (K)	MOPD (cm)	SNR_{RMS}	f_{HDO}
1	0.1034(2)	0.249(1)	293.7(2)	180	1650	–
2	2.9655(65)	0.249(1)	292.2(2)	180	1570	–
3	8.826(17)	0.249(1)	293.5(2)	180	1350	–
4	17.614(45)	0.249(1)	294.4(2)	180	1960	–
5	0.1974(2)	14.556(15)	295.86(10)	250	1470	0.878(22)
6	0.9620(6)	14.556(15)	295.86(10)	250	1490	0.8975(32)
7	4.9626(31)	14.556(15)	296.86(10)	180	1760	0.8911(17)
8	20.000(49)	14.556(15)	295.86(10)	180	1710	0.8915(10)
9	0.1989(2)	72.082(72)	295.87(10)	250	990	0.9189(51)
10	0.9925(6)	72.082(72)	295.87(10)	180	980	0.8916(16)
11	4.9651(31)	72.082(72)	295.86(10)	180	1330	0.90023(66)
12	20.000(49)	72.082(72)	295.87(10)	180	1400	0.90660(34)
13	0.9928(6)	174.61(17)	295.86(10)	180	330	0.8302(18)
14	4.9655(31)	174.61(17)	295.87(10)	180	320	0.9001(11)
15	20.000(49)	174.61(17)	295.87(10)	180	320	0.89628(62)

100 mbar. The gauges were controlled and their readings logged using mks PR4000B pressure readout instruments. The multi-reflection cell measurements were performed with a continuous flow of water vapor through the cell in order to keep the water content in the cell constant during the measurements. The liquid water reservoir is connected to the cell's inlet via a pressure controlled valve keeping the pressure inside the cell at the desired level. The flow rate is controlled via a valve located downstream at the exit connection of the cell. This valve was previously calibrated using a stream of dry nitrogen in combination with an mks mass flow controller. During the water measurements the liquid water reservoir was continuously stirred and heated with a magnetically coupled stirrer combined with a hot plate. Prior to the measurements low resolution empty cell background spectra were recorded. After measurement of these reference spectra the water vapor flow was started and after about 30 min the measurement was started. As for short cell measurements several consecutive blocks were recorded.

2.4.4. Overview of H_2O measurements

In total 15 measurements of pure water vapor absorption spectra at ambient temperature were recorded. The pressures lie between 0.1 and 20.0 mbar, the absorption path lengths between 24.9 cm and 174.6 m. The measurement conditions are summarized in Table 2. Most empty cell measurements were performed with a maximum optical path difference (MOPD) of 9 cm. Some were done with the same MOPD as the sample measurements in order to assess absorption by residual water vapor inside the spectrometer (see Section 3.3).

2.4.5. Characterization measurements

Several measurements of N_2O absorption spectra at low pressures were recorded in order to characterize the ILS and for wavenumber scale calibration. Line position values by NIST [19] in the spectral range 2400–2610 cm^{-1} measured with a heterodyne instrument were used as line position reference. The strong ν_3 absorption band in the spectral range 2180–2260 cm^{-1} can be used for ILS characterization. N_2O measurements were performed under the same measurement conditions as the H_2O measurements. The pressure was about 0.1 mbar for short cell measurements and a few μbar for multi-reflection cell measurements.

3. Spectrum processing

All interferograms were transformed using the OPUS software by Bruker Optics applying a zero filling factor of two and a Mertz phase correction. Transmittance spectra were calculated by dividing sample gas spectra by empty cell background measurements. Before doing the transmittance calculation, the background spectra had to be processed because of residual water vapor

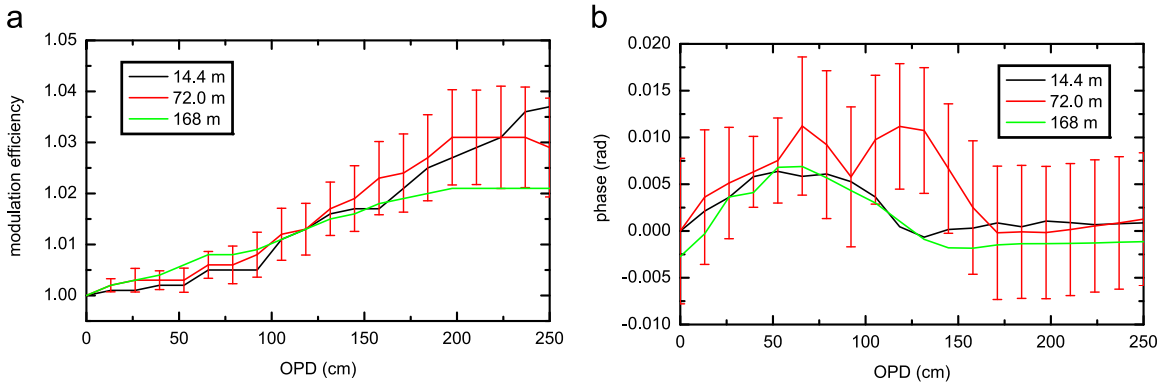

Fig. 2. Example of fitted modulation efficiency (a) and phase (b) at different absorption path lengths of the multireflection cell. The modulation efficiency is defined as relative deviation from the theoretical self-apodization of a Fourier-Transform instrument. For reasons of clarity error bars are only given for one absorption path length. The error magnitude for the other absorption path lengths is similar.

absorption, leading to broad, ringing features in the empty cell reference spectra caused by the low resolution.

3.1. Instrumental line shape characterization

Because of the instrumental line shape's spectral dependence, the spectral range of interest (1850–4000 cm^{-1}) was split into two sections: (1.) 1850–2850 cm^{-1} and (2.) 2850–4000 cm^{-1}. For each section the ILS was characterized using Doppler-broadened absorption lines analyzed with the software LINEFIT 14.5 [20]. This software fits absorption lines by adjusting optical path difference (OPD) dependent modulation efficiency and phase. For ILS characterization for the first wavenumber section Doppler-broadened N_2O lines of the ν_3 vibrational band were used. For the second section H_2O absorption lines at about 3500 cm^{-1} and N_2O $10°1 < 00°0$ lines were used for short and multireflection cell ILS characterization, respectively. As an example, Fig. 2 gives the retrieved modulation efficiency and phase for Section 1 and different absorption path lengths in the multireflection cell. The modulation efficiency shown is defined as relative deviation from the theoretical self apodization.

3.2. Wavenumber calibration

For calibration of the wavenumber scale, Doppler broadened measurements of N_2O $02°1 < 00°0$ vibrational band absorption lines, recorded in the short cell and the multireflection cell, were analyzed using the previously determined ILS. In the analysis, line intensities and line positions were fitted. The retrieved positions were compared to reference positions from NIST [19] and calibration coefficients were determined utilizing a weighted least squares fit. The use of the retrieved calibration factors lead to self-consistent results in a following multispectrum fit of all water vapor absorption spectra. However, during the analysis (see Section 4 for details) systematic differences in water line positions compared to HITRAN12 values were noticed and indicated calibration issues. The systematic deviations were different for the two sections. Since different ILS parametrizations were used for the two regions and the calibrations coefficient was determined from positions of lines in region 1, insufficient transferability of wavenumber calibration when using different ILS parametrizations was presumed as a possible cause. A constant slope of the ILS-phase as a function of OPD is equivalent to a shift of line position and thus, the use of different ILS parametrizations with a common calibration coefficient may lead to inconsistent results. For this reason, the spectra were recalibrated using a spectrum containing N_2O as well as H_2O lines for Section 1. The lines were fitted and the retrieved N_2O line positions were compared to NIST data, resulting in a recalibration coefficient. The recalibrated retrieved H_2O line positions from this spectrum were from then on used as reference positions. For Section 2 HITRAN12 H_2O line positions were used as reference and the spectra were recalibrated. After finishing the analysis, some water vapor absorption spectra in the spectral range 3800–4500 cm^{-1} became available.[1] These spectra had been calibrated using CO absorption lines as reference. In the overlapping spectral range (3800–4000 cm^{-1}) the retrieved line positions were compared to the recalibrated ones. The mean relative difference between the positions was -3.27×10^{-9} with a standard deviation of 3.09×10^{-7}. Because of the wavenumber calibration issues, all line positions retrieved in this study are considered to have a worst case correlated relative error of 10^{-8}.

[1] These spectra were dedicated for retrieval of spectroscopic parameters for the TROPOMI instrument on ESA's Sentinel – 5P satellite.

3.3. Residual water features

Absorption features caused by residual water vapor inside the interferometer were present both in empty cell and sample gas measurements. Residual water features in low resolution empty cell background spectra were fitted effectively using a Voigt function, adjusting line positions, intensities and Lorentz widths. The resulting effective spectral data were used for a forward calculation of background absorption features. The water vapor absorption features were removed from the empty cell spectra by dividing the background measurements by the forward calculation.

In case of sample gas measurements in the multireflection cell the absorption caused by residual water in the interferometer was negligible because the spectra of lines strong enough to be visible in the empty cell measurements were opaque and thus, the interferometer water absorption was not visible. In case of short cell measurements the residual water spectrum had to be considered. For sample spectra where high resolution empty cell spectra were measured, these were used for transmittance calculation. For the other spectra synthetically high resolved empty cell spectra were calculated as follows. Starting from a high resolution background measurement, effective line parameters (DB_{HR}) were fitted using a Voigt line profile. The same measurement's interferogram was transformed with the resolution limited to the one used for low resolution background spectra. From this low resolution spectrum another set of effective line parameters (DB_{LR}) was retrieved. In order to calculate synthetically high resolved background spectra, the water lines in the low resolution spectrum of interest were fitted and the water features removed (as explained above). By comparing the fitted effective intensities with DB_{LR} a scalar scaling factor was determined and a high resolution absorption spectrum was calculated using DB_{HR} and the scaling factor. By multiplication of the forward calculations with corrected low resolution background measurements synthetically high resolved empty cell measurements were calculated. These measurements were used for transmittance calculation.

3.4. Channelling correction

Because of Fabry-Perot effects, for instance caused by internal multireflection of the beam in the optical filter, channeling was present in the measured spectra. If the channeling is constant for reference and sample spectra, it cancels out when doing the transmittance calculation. In some cases, particularly for White cell measurements, this was not the case and residual channeling was present in transmittance spectra. In such cases the wavenumber scale of the reference spectra was scaled to minimize channeling effects in transmittance spectra. This treatment leads to a slight change of the 100% baseline which is fitted in the line parameter analysis anyway.

3.5. Contaminations and isotopologue abundances

Besides water absorption, absorption by CO_2 was also present in the spectra. These contaminations are ascribed to residual dissolved CO_2 content in the liquid water sample that could not be removed completely. The strongest absorptions by CO_2 lie between 2200 and 2400 cm^{-1} as well as 3550 and 3750 cm^{-1} with the highest intensity above 3.5×10^{-18} cm $molecule^{-1}$. Because of continuous evaporation and flow through the cell, the CO_2 content did not stay constant during the measurements. In this case, strong lines cannot be modelled using, for instance, an effective Voigt line shape model because of the nonlinearity of Beer's law. Because of this, the region with highest absorption by CO_2 (2280–2390 cm^{-1}) was excluded from the analysis. CO_2 lines outside this region of strong absorption were fitted using a Voigt line shape

model, adjusting line positions, intensities and Lorentz widths. With these effective parameters the spectra were corrected for absorption by CO_2. The CO_2 partial pressure in the sample gas was in all cases below 0.7 μbar. In two spectra minor absorption, corresponding to a partial pressure of 5.6 nbar, by OCS was present. These contamination features were removed in the same way as the CO_2 absorption. This approach is justifiable because of the high resolution and hence the small width of the ILS.

During the measurements liquid water was evaporated continuously. Because of the different vapor pressures of water isotopologues, the gas phase composition is changing slowly. This effect is particularly crucial for HDO with a vapor pressure about 8% lower than $H_2{}^{16}O$. For this reason, single spectrum fits of all measured spectra were performed and effective HDO intensities retrieved. Using these intensities an HDO column scaling factor was fitted using HITRAN12 HDO intensities as reference. The determined factors f_{HDO} are listed in Table 2.

4. Line parameter retrieval

A multispectrum fitting software [21] written in IDL (Interactive Data Language by Exelis Visual Information Solutions, Inc.) was used for all performed line parameter retrievals. The tool is capable of performing microwindow-based interactive and automated multispectrum fits making use of several line shape models, including the Hartmann-Tran-Profile (HTP) [22–25]. This profile takes velocity changing collisions (Dicke-effect, ν_{VC}), speed-dependences (Γ_2, Δ_2) of broadening (Γ_0) and shift (Δ_0) as well as a correlation (η) between velocity changing and internal state changing collisions into account. It has been extended to account for line mixing in the Rosenkranz first order perturbation approximation (Y) [10], according to $I(\sigma)=RE[K(\sigma)]+Y\,IM[K(\sigma)]$, with K being the complex line shape model. Assuming binary collisions the collisional parameters are linear in pressure. During the analysis it turned out that the fit of positions σ, intensities S and the line shape parameters $\gamma_{0,s}$, $\gamma_{2,s}$, $\delta_{0,s}$ and Y_s were necessary to model the measurements to the noise level. All other non-Voigt parameters were set to zero. The used line shape model was thus a quadratic speed-dependent Voigt with line mixing.

The analysis of the spectra was done iteratively, starting with multispectrum fits of short cell measurements. After completion of the short cell measurements, spectra with the next higher absorption path length were included, and so on. Resulting parameters from previous steps were set as initial parameters in the subsequent iteration. All parameters fitted in a previous iteration were fitted in every subsequent analysis step. HITRAN12 was chosen as a starting point. The HITRAN parameters were used as initial guess for fitted parameters and kept constant for parameters not fitted. All HITRAN lines with a minimum absorption of 20% of the RMS-Noise in at least one measurement were considered in the calculations. Microwindow boundaries were chosen automatically according to

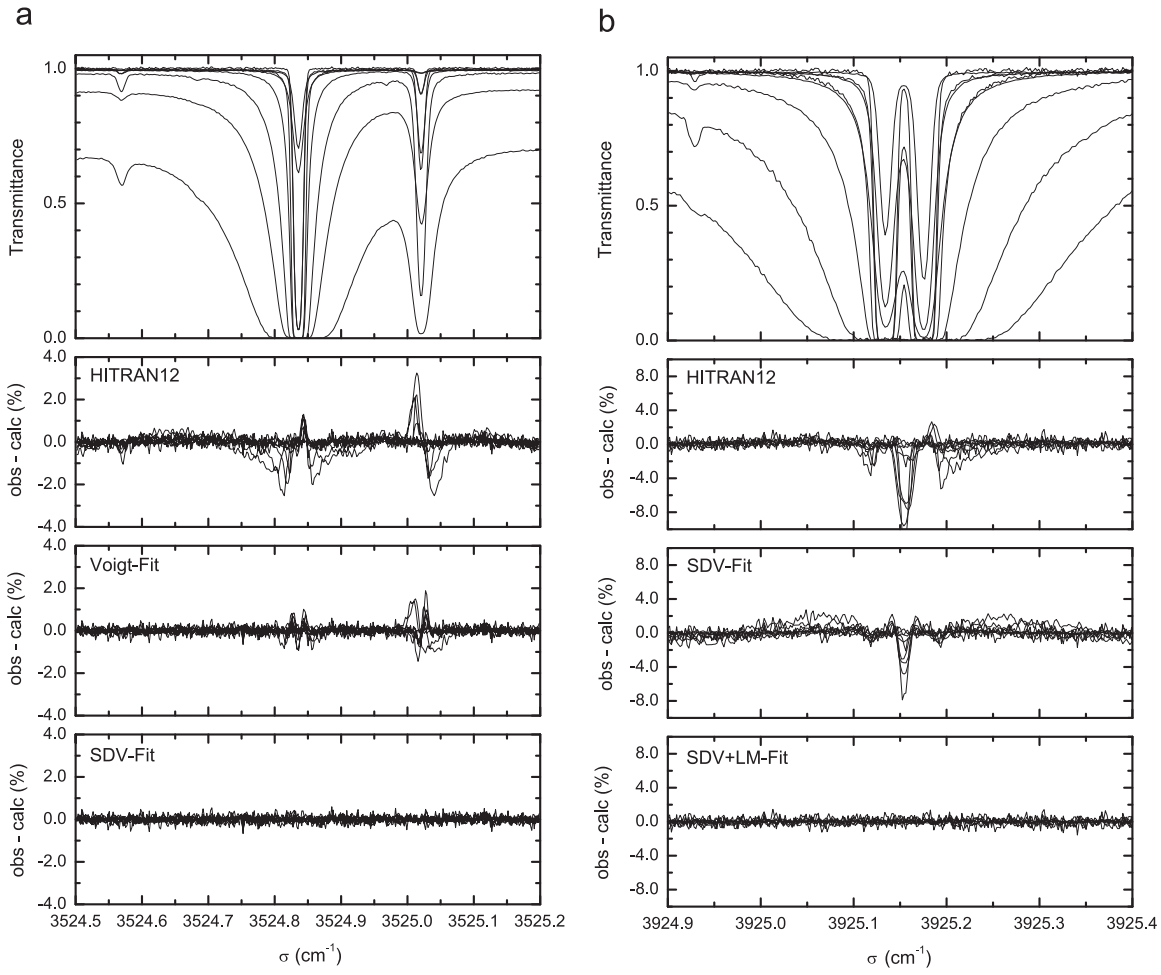

Fig. 3. Two exemplary sections of fitted microwindows together with residuals of fits using different line shape models. For reasons of clarity only spectra with visible absorption are shown. The residuals are labelled as follows. HITRAN12: forward calculation using the HITRAN12 line parameters; Voigt-Fit: Fit of line position, intensity and self-broadened width; SDV-Fit: additional fit of speed-dependence and self-shift; SDV+LM-Fit: additional fit of self-line mixing in the Rosenkranz approximation. By using non-Voigt line shape models the measurements could be fitted to the noise level simultaneously.

spectral point of maximal transmittance in the spectrum with the highest water column while at the same time keeping the microwindow width between 0.25 and 0.75 cm^{-1}. The 100%-level was fitted for every spectrum and each microwindow as a 2nd order polynomial. For temperature conversion of line intensities the total internal partition sum [26] was used.

The lines were fitted using the abovementioned HTP line profile implementation with Rosenkranz line mixing. The line parameters to be fitted were chosen in the following way: Every line was categorized according to its maximum peak absorption in units of the local root mean square (RMS)-noise. If the maximum peak absorption was above 5 × RMS-noise, the line is labelled as "visible", above 25*RMS-noise as "clearly visible" and above 100 × RMS-Noise as "dominant". For "visible" lines positions and intensities were fitted, for "clearly visible" lines self-broadening was fitted additionally. For "dominant" lines speed-dependence was adjusted, too. The self-shift parameter was fitted if the line was "clearly visible" in at least two spectra with a minimum pressure difference of 1 mbar. After each fit, parameters with statistical errors above 100% were unselected and the fit was redone, keeping these parameters at their initial values. In the case of high parameter correlations (correlation coefficient above 0.99), one of the two correlated parameters was unselected for the next fit. If the two parameters belonged to separate lines, the weaker line's parameter was unselected. If the correlated parameters belonged to a single line, one parameter was unselected according to the order Y_s, $\delta_{0,s}$, $\gamma_{2,s}$, $\gamma_{0,s}$, S, σ. After each automatic fitting round the residuals were visually inspected on microwindow basis and failed microwindows were identified and refitted manually. If asymmetric residuals were visible, the line mixing parameter Y_s was fitted additionally. Fig. 3 gives an example of the fitting of two microwindows using different line shape models. In the upper panels, the measured transmittance is shown, in the subsequent panels the residuals for a forward calculation using HITRAN12 and fits using different line shape models are shown.

5. Error analysis

An extensive error propagation analysis was performed for every fitted parameter of each line. Besides the calibration error which was quantified in Section 3.2 and the statistical error which is part of the output of the fitting procedure, contributions of systematic error sources were investigated. Causes of systematic errors are inaccuracies of temperature and pressure measurement as well as the inaccuracy of the absorption path. Additionally, the influence of the ILS parametrization inaccuracy was studied extensively. The last error source investigated is the contribution of the self-temperature dependence parameter n_s. Each error source might be line- and spectrum-specific. For example, an error in the absorption path length of the used short cell does not influence the retrieved intensities of weak lines. The intensity information of such lines originates only from multireflection cell measurements. The information contribution I_{sp} of a spectrum s to a fitted parameter p can be calculated [27] by

$$I_{sp} = \frac{\sum_{n_s} \left| \left(CA^T W \right)_{p,n_s} \right|}{\sum_{n=1}^{N} \left| \left(CA^T W \right)_{p,n} \right|}$$

C denotes the covariance matrix, A is the Jacobian and W is the data point weight vector. CA^TW is a $P \times N$ matrix, where P is the number of fitted parameters and N is the total number of spectral points. The enumerator summation goes over each spectral point of spectrum s (in the microwindow of interest). Measurement errors were propagated in the following way.

5.1. Pressure, temperature and absorption path length inaccuracies

From the inaccuracies of pressure and temperature measurement as well as the absorption path length virtual spectrum specific parameter errors were calculated. The relative error of a pressure measurement is directly propagated into the error of line intensity and line shape parameters whereas a path length error affects only retrieved intensities. An inaccuracy in temperature affects line intensities via the calculation of number densities and via intensity temperature conversion. Intensity temperature conversion errors were estimated by converting retrieved intensities (at reference temperature) back to measurement temperatures, changing the measurement temperature and reconverting to reference temperature. The resulting difference to the original reference temperature line intensity is used as the error. Temperature dependence of widths, speed-dependence and shifts was not considered in the analysis. To access the error made by this approach, the differences between the retrieved parameters and those converted from measurement temperature to reference temperature, assuming a power law and a temperature exponent of 0.7, was assumed to be a good estimation of this source of inaccuracy. From the virtual spectrum specific errors the propagated systematic errors from multispectrum fitting were estimated as a weighted mean or weighted quadratic mean of the virtual errors where the weights were set to the abovementioned information contribution I_{sp}. Correlated errors were propagated with the weighted mean, uncorrelated errors by calculating the square root of the weighted quadratic mean.

$$\sigma_p = \frac{\sum_s I_{sp}\sigma_{sp}}{\sum_s I_{sp}} \quad \text{for correlated errors}$$

$$\sigma_p = \sqrt{\frac{\sum_s I_{sp}^2\sigma_{sp}^2}{\sum_s I_{sp}^2}} \quad \text{for uncorrelated errors}$$

Apart from pressure measurements at different pressures or values originating from different measurement devices, all error sources were considered as correlated.

5.2. ILS errors

In order to assess the error introduced by inaccuracies of the ILS parametrization, the whole analysis was redone for each used ILS parametrization where the ILS was distorted in a certain way. Modulation efficiencies (as a function of OPD) were distorted by adding a straight line. The distortion's magnitude is specified by the straight line's slope. The phase distortion was done by adding a constant value. The magnitudes of the distortions introduced through this process were determined in the following way: If there was no error in ILS parametrization, the χ^2 value of every fitted microwindow should be at its minimum. A representative selection of microwindows was fitted with different distortion magnitudes. The χ^2 value happened not to be at its minimum for the fit using the nominal ILS parametrization. Instead, the distortion with minimum χ^2 value showed some scatter. An example of χ^2 as a function of modulation efficiency distortion for a selection of microwindows is shown in Fig. 4. The maximum distortion with minimal χ^2 value was chosen as a worst case, i.e. 0.02 m^{-1} in the example. The differences in resulting parameters (with nominal and distorted ILS) were considered as the parameter errors introduced by ILS parametrization inaccuracy.

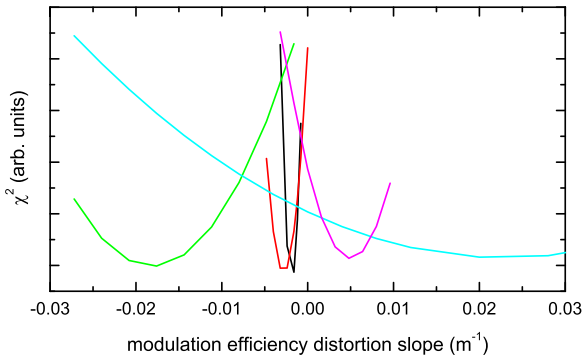

Fig. 4. Example of χ^2 as a function of modulation efficiency distortion for a selection of microwindows. The colors indicate different microwindows.

5.3. Total errors

Errors originating from several error sources were propagated or estimated for each parameter. Although these errors are of different nature and the calculation of a single total error is strictly speaking not reasonable, a total error was calculated by calculating the root mean square value.

Fig. 5 shows, as an example, the errors for line intensities. From the behavior of errors caused by pressure, temperature and absorption path length inaccuracies a transition of main information spectra from short cell to multireflection cell spectra at about 2×10^{-22} cm molecule^{-1} can be seen. It is emphasized that the error introduced by inaccuracies of the ILS parametrization is the dominant systematic error source for strong lines and highly variable for weak lines. Fig. 6 shows the propagated errors for self-broadening parameters. As for line intensities, the inaccuracy of the ILS parametrization is in most cases the dominant systematic error source.

5.4. Parameter redundancy and goodness of fit

Since measured transmittance spectra might be affected by systematic errors not accounted for in the error estimation, it was made sure that the measurements provided sufficient redundant information on the retrieved line parameters. For every retrieved line parameter the redundancy (Eq. (5) in [12]) is calculated by the software. The redundancy is a measure of the number of virtual statistically independent measurements of equal information content that contributed to the corresponding parameter. High redundancy helps minimizing systematic errors and gives confidence in the fit. The mean redundancies of the retrieved parameters lie between 2.5 and 2.8.

To assess the goodness of fit, the reduced χ^2 value was calculated for every fitted microwindow. In case of good modelling of the spectra the reduced χ^2 is about 1 whereas lower or higher values indicate overfitting or insufficient modelling, respectively.

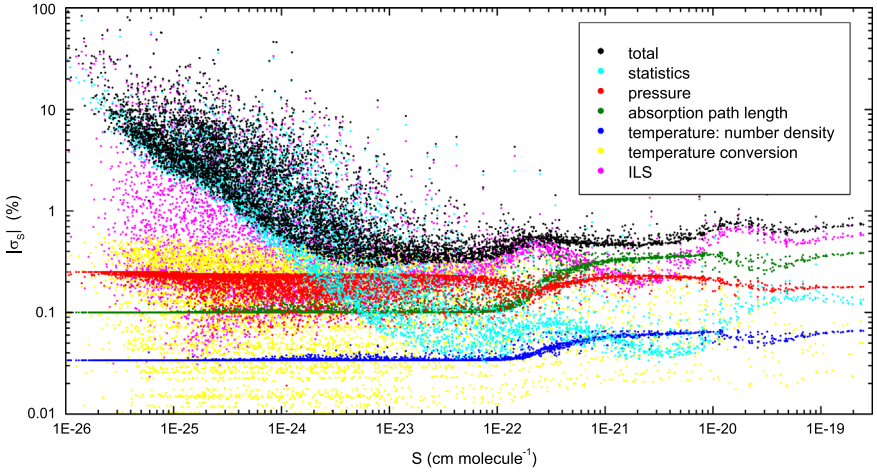

Fig. 5. Propagated line intensity inaccuracies for different error sources. For every line the influence of all measurement errors is propagated. The error due to some error sources does not show a large variability, whereas the retrieved line intensity sensitivity to ILS errors is highly variable.

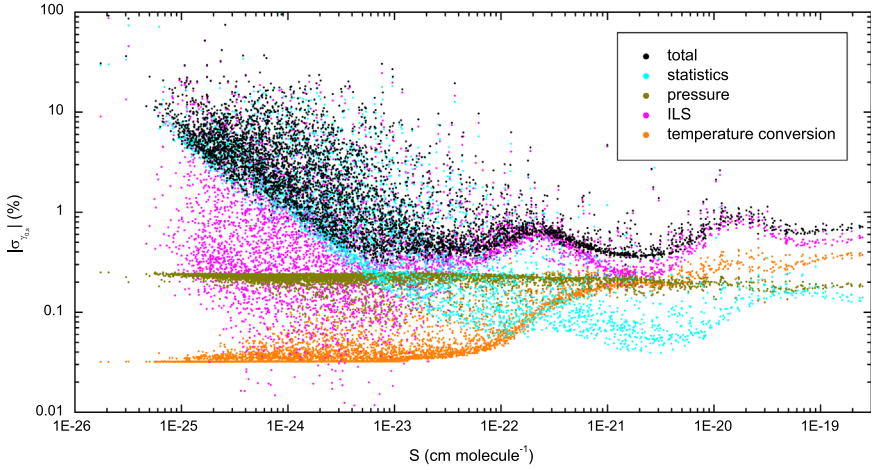

Fig. 6. Propagated self-broadening inaccuracies for different error sources. For every line the influence of all measurement errors is propagated.

Due to its nature the reduced χ^2 value is subject to a certain level of scatter. Therefore, the distribution of all obtained values was investigated. The mean value and the standard deviation were 0.971 and 0.080, respectively, and thus suggest adequate fitting.

6. Broadening parameters from saturated lines

Typically, in laboratory spectroscopy saturated lines were avoided due to a large correlation of line intensity and line broadening as well as a high sensitivity to systematic errors. Small changes in the transmittance in opaque regions cause large changes in the optical depth due to the exponential dependence of transmittance and optical depth and are thus the reason for the high sensitivity to systematic errors and perhaps noise. In the following, it will be shown that the use of opaque regions in the fitting does not necessarily cause problems.

In order to assess the impact of using saturated regions in line parameter determination, a Monte-Carlo analysis was performed fitting 100 synthetic transmittance spectra of a single test line. The noise level corresponded to the noise level of spectra used in the analysis. The absorption path was set to 0.249 m and the partial pressure to 9 mbar. In a first run, the whole spectral range was considered in the fits. In a second run, only spectral regions with optical depths <4 were taken into account. In the fits only the self-broadening parameter was adjusted. It turned out that noise from high optical depth regions does not influence the retrieved parameter. The broadening parameter differed by only 0.05%. The statistical error given by the fit represented the standard deviation of the retrieved parameters correctly. In order to assess the systematic error caused by deviations of the zero level, an additional Monte-Carlo run was performed with an offset of 0.02% added to the zero level. Such a deviation could be caused by detector nonlinearity and the magnitude applied was based on recent experience on nonlinearity of the internal InSb detector. The systematic difference found in this run was -0.03% with respect to the run without zero level offset.

The errors found in this investigation are, in comparison to other error sources, rather small. It is important, though, when using saturated lines for retrieval of broadening parameters, to include unsaturated measurements in the multispectrum fitting in order to eliminate the high correlation of line intensity and line width.

Opaque lines can be used to obtain additional information compared to non-opaque lines which was described in detail in the publication of Birk and Wagner [9].

A measure of information content for fitted parameters is given by

$$I = \left(A^T W A\right)^{-1} A^T W$$

A denotes the Jacobian and W is the vector containing the weights. The information contribution to the self-broadening parameter is shown – as an example – for a synthetic high intensity saturated line in Fig. 7. As can be seen from the lower panel, data points of high optical depth do not carry any information. On the other hand, information from the line wing is available where the location of the information maximum with respect to the line center can be influenced by the peak optical depth. Thus, the peak optical depth can be used to tune to a certain region in the line wing which can be advantageous when investigating, for example, far line wings without suffering from model errors close to the line center. Saturated lines appear also in atmospheric spectra. The use of spectroscopic parameters determined from non-saturated lines for modelling of these lines is an extrapolation because of the different weighting of information (see Birk and Wagner [9]). Therefore, saturated lines should also be included in the laboratory spectroscopy.

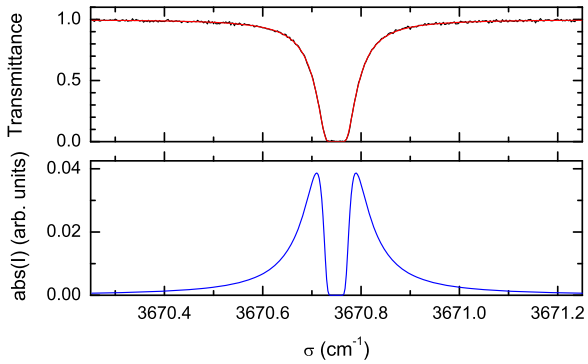

Fig. 7. Measured (black) and fitted (red) transmittance of a synthetic high intensity line. The information content is shown in blue. Due to vanishing Jacobian entries the information contribution for spectral ranges with high optical depth are close to zero. (For interpretation of the references to color in this figure legend, the reader is referred to the web version of this article.)

In the present study even in the measurement with the lowest column with still sufficient pressure for significant self-broadening contribution (measurement #2 in Table 2), strong lines with intensities above 10^{-19} cm molecule^{-1} were saturated. Thus, for retrieval of self-broadening parameters only the line wings contributed to a considerable amount. However, spectral regions with high optical depths were not excluded by the fitting algorithm. According to the statements above, saturated lines can be used for determination of pressure broadening parameters and, moreover, the use of saturated lines can be advantageous.

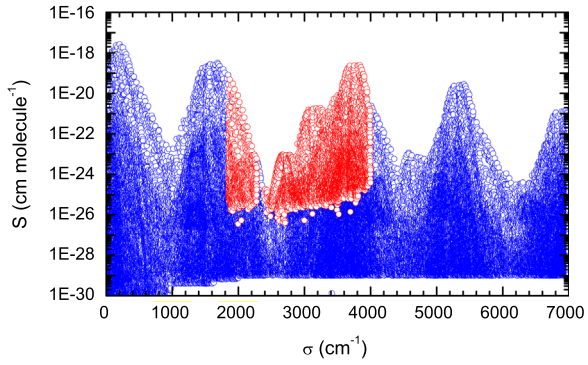

Fig. 8. Overview of the fitted lines (red) in the infrared absorption spectrum of water vapor (blue, HITRAN12). (For interpretation of the references to color in this figure legend, the reader is referred to the web version of this article.)

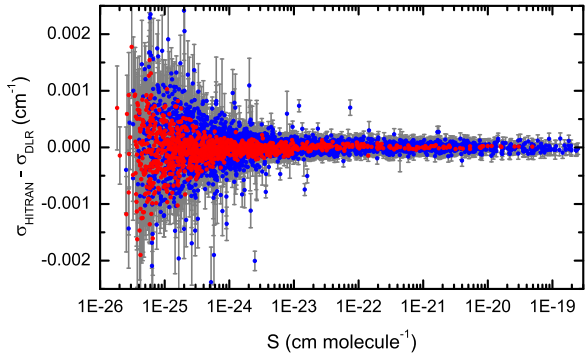

Fig. 9. Comparison of retrieved line positions to HITRAN12 values. red: Section 1 (1850–2850 cm^{-1}), blue: Section 2 2850–4000 cm^{-1}). Only positions with HITRAN error of 0.0001 cm^{-1} or better are shown. Combined error bars are shown in grey. (For interpretation of the references to color in this figure legend, the reader is referred to the web version of this article.)

Table 3
Number of fitted line parameters. Note that for non-main isotopologue lines the intensities are to be considered as relative.

Isotopologue	Parameter				
	σ	S	$\gamma_{0,s}$	$\gamma_{2,s}$	$\delta_{0,s}$
$H_2{}^{16}O$	4016	4002	3323	2678	2574
$H_2{}^{18}O$	1036	1034	739	500	477
$H_2{}^{17}O$	622	620	396	241	211
HDO	1300	1291	841	509	456
Total	6974	6947	5299	3928	3718

7. Results and discussion

Table 3 gives the number of parameters retrieved. Note that intensity values of non-main isotopologues are only known on a relative basis because of unknown isotopic composition of the measured sample gas. Fig. 8 gives an overview of the fitted lines and their location in the absorption spectrum of water vapor. The spectral range analyzed is 1850–4000 cm^{-1} with exclusion of the range 2280 to 2390 cm^{-1}. The distribution of the parameters in HITRAN error categories is given in Tables 4 and 5. In the following sections combined error bars are given for parameters compared with values of other sources. These errors are formed by calculation of the root sum of squares of the total errors given in this work and the corresponding error of the other source. In case of HITRAN values the upper error range limit is used.

Table 4
Distribution of retrieved line intensities, widths and speed-dependence in HITRAN error categories. Speed-dependence parameters $\gamma_{2,s}$ are not part of HITRAN12 and the same categories as for $\gamma_{0,s}$ are used.

Error category	8	7	6	5	4	3
error range (%)	<1	<2	<5	<10	<20	≥ 20
# S (%)	46.0	12.8	24.1	13.2	2.8	1.1
# $\gamma_{0,s}$ (%)	41.8	15.4	24.9	14.1	3.9	0.7
# $\gamma_{2,s}$ (%)	0.0	0.0	9.1	34.1	24.9	31.9

Table 5
Distribution of retrieved line positions and self-shift parameters in HITRAN error categories. Self-shift parameters $\delta_{0,s}$ are not part of HITRAN12. The same categories as for σ are used.

Error category	6	5	4	**3**	2	1
error range (cm^{-1} or cm^{-1} atm^{-1})	$<10^{-5}$	$<10^{-4}$	$<10^{-3}$	$<10^{-2}$	$<10^{-1}$	$\geq 10^{-1}$
# σ (%)	16.0	38.7	43.6	1.6	0.1	0.0
# $\delta_{0,s}$ (%)	0.0	0.0	26.0	63.7	10.2	0.1

7.1. Line positions

Positions have been determined for 6974 lines with the majority of parameter errors below 0.0001 cm^{-1} if the calibration error of 10^{-8} is not considered. A comparison to HITRAN12 values is shown in Fig. 9. Line positions in the first and second spectral

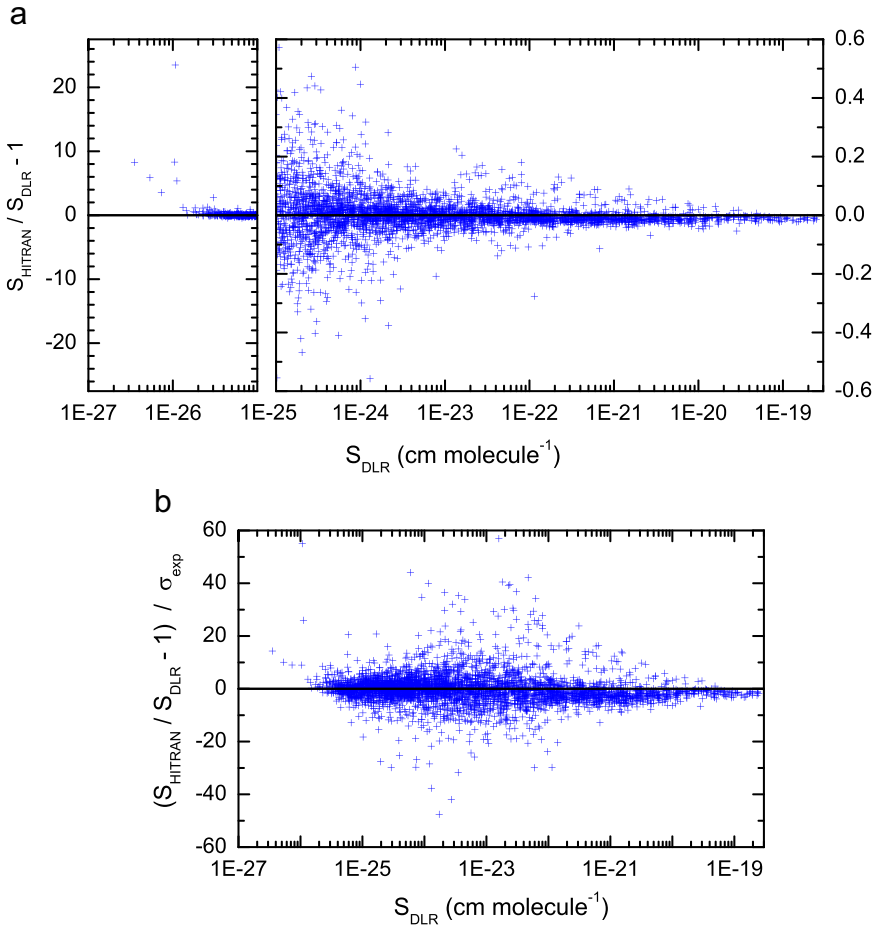

Fig. 10. Comparison of retrieved $H_2{}^{16}O$ line intensities to HITRAN12. (a); the scale of the left panel was extended to show all data points. (b) Relative differences in units of experimental errors.

region are shown in red and blue. The comparison is only done for HITRAN values with specified accuracy better than 0.0001 cm^{-1}. The majority of positions are in good agreement with HITRAN values which are based on the work of Toth et al. [28].

7.2. Line intensities

Absolute line intensities have been retrieved for about 4000 main isotopologue lines and relative intensities for about 3000 $H_2{}^{18}O$, $H_2{}^{17}O$ and HDO lines. The majority of retrieved intensities is in the range 3×10^{-26}–3×10^{-19} cm $molecule^{-1}$. The distribution in HITRAN error categories is given in Table 4. The specified total error of most intensities is below 1%.

7.2.1. Comparison to HITRAN12 and GEISA15

The retrieved main isotopologue intensities were compared to HITRAN12 and GEISA15 [29]. The relative differences are given in Figs. 10a and 11a. Whereas HITRAN values are mostly from the work of Toth et al., GEISA intensities are based on semi-empirical calculations. For both HITRAN and GEISA relative deviations of over 50% are present for intensities below 10^{-24} cm $molecule^{-1}$. For intensities above 10^{-23} cm $molecule^{-1}$ HITRAN shows a larger scatter than GEISA. There is a systematic difference of about -1.5%, most visible for large intensities, in both cases. For intensities below 10^{-26} cm $molecule^{-1}$ some HITRAN values deviate by a factor of up to 20. Relative differences in units of experimental errors are shown in Figs. 10b and 11b indicating that for many lines the deviations are not due to experimental scatter.

7.2.2. Comparison to experimental values

The intensities were compared to the work of Mikhailenko et al. [30], Ptashnik et al. [31] and Pogany et al. [32]. The values by Mikhailenko et al. (intensities between 10^{-26} and 2×10^{-23} cm $molecule^{-1}$) are based on Fourier-Transform measurements. The comparison is shown in Fig. 12. There are deviations of over 80% and a certain structure visible above 5×10^{-24} cm $molecule^{-1}$. This structure is also visible when comparing Mikhailenko's values to calculations by Partridge and Schwenke (Fig. 1b in [30]). A comparison to FTS intensities of Ptashnik et al. and Pogany et al. is given in Fig. 13. Apparently, the values do not only agree within their combined error bars but show an almost perfect agreement for intensities above 2×10^{-20} cm $molecule^{-1}$. For this intensity range the weighted mean deviation is only –0.12%.

7.2.3. Comparison to ab initio calculations

An extensive comparison of experimental $H_2{}^{16}O$ line intensities from FTS measurements at DLR and *ab initio* calculations by Tennyson's group at UCL [33] is given in a separate publication [34]. This comparing paper includes also lines in the spectral ranges 1250–1750, 4190–4340 and 1000–11000 cm^{-1} by Birk et al. For this reason only a brief overview and the major findings are given at this point. Fig. 14 gives an overview of the deviations of measured and calculated intensity values. The *ab initio* values were scaled using the natural abundance of $H_2{}^{16}O$. The agreement of FTS data is considerably better with *ab initio* than with HITRAN12 or GEISA15 but there seem to be several lines with above-average deviations. These high deviations might be due to local resonances not

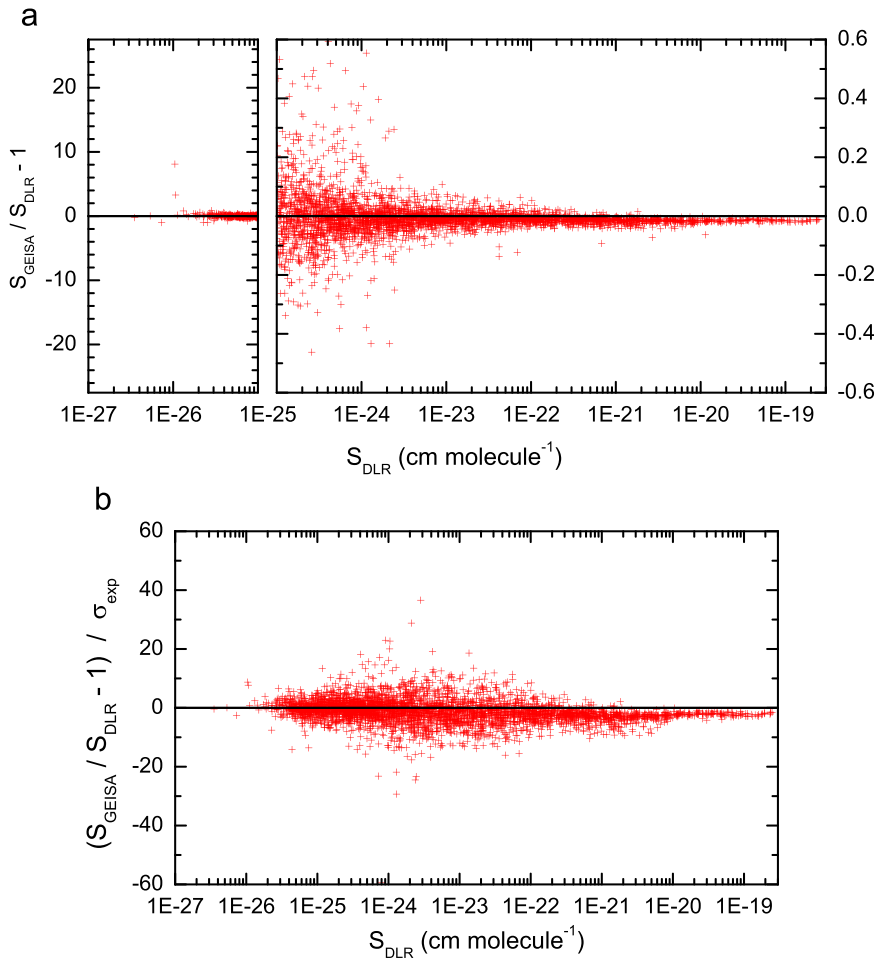

Fig. 11. Comparison of retrieved $H_2{}^{16}O$ line intensities to GEISA15. (a) Relative differences; the scale of the left panel was extended to show all data points. (b) Relative differences in units of experimental errors.

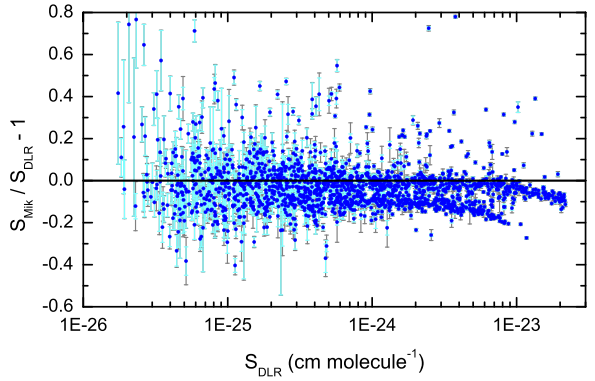

Fig. 12. Comparison of retrieved line intensities to Mikhailenko et al. [30]. Combined error bars are given in grey, the errors of values from this work in cyan. Mikhailenko et al. only report statistical errors. (For interpretation of the references to color in this figure legend, the reader is referred to the web version of this article.)

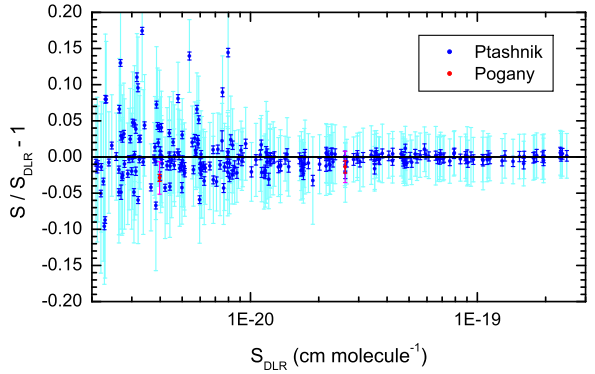

Fig. 13. Comparison of retrieved line intensities to Ptashnik et al. [31] (blue) and Pogany et al. [32] (red). Combined error bars are given in cyan and magenta, the errors of values from this work in blue and red. (For interpretation of the references to color in this figure legend, the reader is referred to the web version of this article.)

modeled correctly in the calculation. Interestingly, exceptionally high deviations of up to two orders of magnitude were noticed for transitions to the rovibrational state $\nu_1\nu_2\nu_3 J_{KaKc}=010,13_{11,2}$. A comparison to *ab initio* data for separated vibrational bands and experimental errors below 1% is given in Fig. 15. Apart from vibrational band dependent systematic differences, there seems to be a vibrational band specific scatter. This is summarized in Table 6. The systematic deviations and scatter are most pronounced for the ν_1 vibrational bands. Systematic differences or scatter specific to vibrational bands cannot originate from experimental errors or inaccuracies. However, there is a remarkable overall agreement between *ab initio* calculations and measured intensities which is below 1% in most cases.

7.3. Self-broadening, its speed-dependence and self-shifts

7.3.1. Overview

Self-broadening parameters were determined for about 5300 lines. Additionally, self-speed-dependence and self-shift coefficients were measured for about 3900 and 3700 lines, respectively. The error distribution in HITRAN categories is given in Table 4. Fig. 16 shows an overview of the determined line shape parameters, plotted versus line intensity. Instead of the speed-dependence parameter $\gamma_{2,s}$, the ratio $\gamma_{2,s}/\gamma_{0,s}$ is shown. The self-broadening parameter $\gamma_{0,s}$ lies between 0.1 and 0.55 cm^{-1} atm^{-1}. This spread is due to the strong dependence of water self-broadening parameters on the vibrational quantum number m ($m=-J''$, J'' and $J''+1$ for P-, Q- and R-branch lines, respectively). The ratio $\gamma_{2,s}/\gamma_{0,s}$ exhibits far less variability indicating a weaker dependence on m. In the intensity range 10^{-24}–10^{-20} cm $molecule^{-1}$ the ratios seem rather constant whereas for low and high intensities larger and smaller values, respectively, were retrieved. This behavior could be due to the different ranges of optical depth of contributing measurements. For high and low intensity lines no measurements of low and high optical depths were available. From this explanation one could conclude that the used line shape model was not representing the measurements sufficiently and maybe the inclusion of collisional narrowing would further improve the fitted parameters. The majority of self-shift coefficients is within ± 0.05 cm^{-1} atm^{-1} without any visible dependence on intensity.

Table 6
Offset and standard deviation of the comparison of retrieved intensities and UCL *ab initio* calculations [34].

vibrational band ($\nu_1\nu_2\nu_3$)	Systematic deviation (%)	Standard deviation (%)	Number of lines
ν_1-bands			
100 – 000	−2.4	3.5	591
110 – 010	−1.4	1.9	19
ν_2-bands			
010 – 000	−0.85	0.80	220
020– 010	−0.51	1.7	23
020–000	−0.68	1.4	539
030–010	−0.57	1.4	34
ν_3-bands			
001 – 000	+0.23	1.8	665
011 – 010	+0.34	0.70	123
combination bands			
001 – 010	+0.02	0.60	54
100 – 010	−1.0	0.73	54

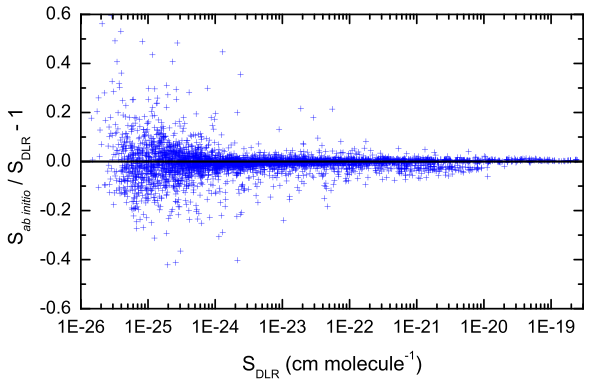

Fig. 14. Comparison of retrieved line intensities to UCL *ab initio* calculations [34].

7.3.2. Comparison to HITRAN12 values

The relative differences of HITRAN12 values to the retrieved self-broadening parameters are given in Fig. 17. The HITRAN data sources are shown in different colors. Most of the parameters are measured values by Toth et al. [28,35,36] and Mandin et al. [37,38] as well as complex Robert-Bonamy calculations by Antony et al. [39]. Toth et al. used either a Voigt line shape or a model including collisional narrowing in the analysis whereas values by Mandin et al. are derived from analytical expressions using peak absorption and intensity measurements or equivalent widths. The parameters by Toth et al. and Antony et al. do not show systematic deviations over 1% whereas values by Mandin et al. exhibit a systematic difference of 18.5%. The scatter is rather large in all cases and a lot of lines show deviations of up to 80%.

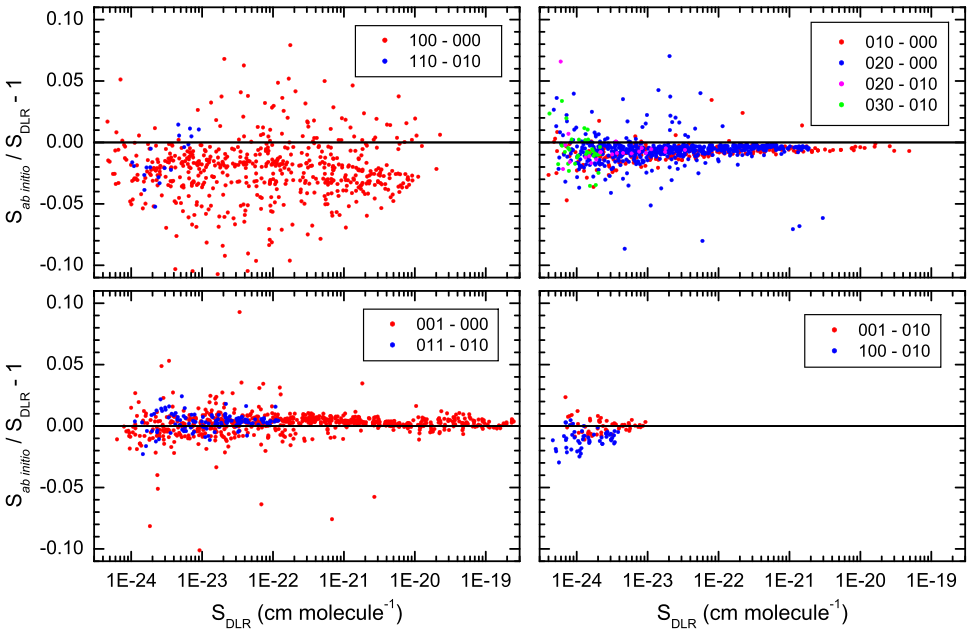

Fig. 15. Comparison of retrieved line intensities to UCL *ab initio* calculations [34] for lines with experimental error below 1%. The different vibrational bands show specific offsets and scatter. (For interpretation of the references to color in this figure legend, the reader is referred to the web version of this article.)

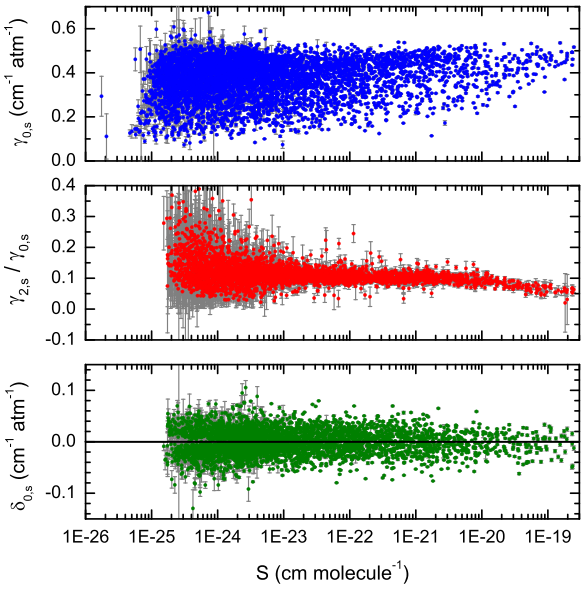

Fig. 16. Overview of retrieved self-broadening parameters $\gamma_{0,s}$, speed dependence $\gamma_{2,s}/\gamma_{0,s}$ and self-shift coefficients $\delta_{0,s}$.

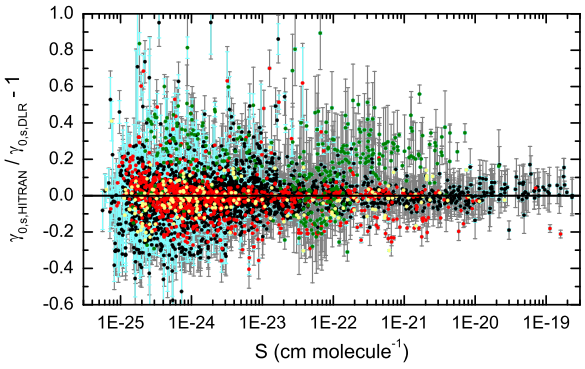

Fig. 17. Comparison of retrieved self-broadening parameters to HITRAN12. Combined error bars are given in grey, errors of this work's parameters in cyan. HITRAN values are based on the work of (black) Toth et al. [28,35,36], (green) Mandin et al. [37,38], (red) Antony et al. [39] and (yellow) others. (For interpretation of the references to color in this figure legend, the reader is referred to the web version of this article.)

7.3.3. *Comparison to Ptashnik et al.*

For large intensities there are recent experimental self-broadening parameters by Ptashnik et al. [31]. The relative differences to this work's results are shown in Fig. 18. The analysis of Ptashnik et al. was done using the Voigt and the Rautian-Sobel'man profiles. Where the Voigt results deviate systematically by −5.6%, the results originating from the analysis using the Rautian profile differ systematically by only −2.5% with noticeably better agreement for intensities above 10^{-19} cm molecule^{-1}. The different systematic deviations confirm the systematic errors introduced by the use of line profiles not accurately representing the measured lines, as observed by Birk and Wagner [9]. For the majority of lines the retrieved parameters agree within the combined error bars with the Rautian values by Ptashnik et al.

7.4. *Line mixing*

Self-line mixing parameters in the Rosenkranz approximation were retrieved for about 150 lines. Self-line mixing parameters Y_s were fitted in addition to the other line parameters in case of asymmetric residua of the fit. The errors of the fitted values were above 20% in most cases and only for a few pairs of lines significantly lower errors were obtained. It turned out that retrieved line mixing parameters respond very sensitively to ILS inaccuracies. An example of rather strong self-line mixing is given in Fig. 3b. The retrieved parameters are plotted versus line positions in Fig. 19. Plotting versus line positions allows for identifying collisionally coupled pairs or groups of lines. Because of the lack of other works on self-line mixing of water vapor a meaningful comparison cannot be made at this point.

8. Summary and conclusion

This work is the first of two publications on water vapor line parameters in the spectral ranges 1850–2280 cm^{-1} and 2390–

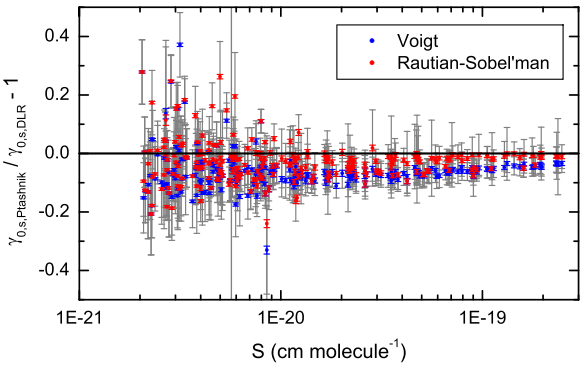

Fig. 18. Comparison of retrieved self-broadening parameters to Ptashnik et al. [31]. Ptashnik et al. give results for analyses using the Voigt (blue) and the Rautian-Sobel'man (red) profile. Combined error bars are given in grey, errors of this work's parameters in blue and red. (For interpretation of the references to color in this figure legend, the reader is referred to the web version of this article.)

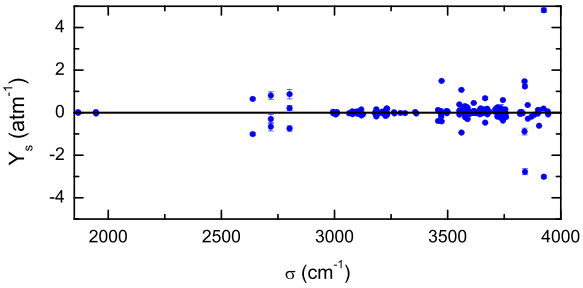

Fig. 19. Retrieved Rosenkranz self-line mixing parameters vs. line positions.

4000 cm^{-1}. It is dedicated to the use in ground based remote sensing of Earth's atmosphere. An experimental dataset containing water vapor line positions, intensities and self-line shape parameters in the intensity range from 3×10^{-26} to 3×10^{-19} cm $molecule^{-1}$ is presented.

A set of pure water FTS transmittance spectra was measured applying high spectral resolution to minimize the ILS influence. The column amount grid was set to give high redundancy and to optimally cover the intensity range needed by the remote sensing community. The measurements were analyzed utilizing a multi-spectrum fitting approach using a quadratic speed-dependent Voigt model extended to account for line mixing in the Rosenkranz first order perturbation approximation. During the fit, positions, intensities, self-broadening, its speed-dependence, self-shift and in some cases self-line mixing parameters had to be adjusted in order to fit the measurements to the noise level. For the retrieved parameters an extensive error estimation calculation was performed and the errors of pressure and temperature measurement, absorption path inaccuracy, ILS parametrization errors and statistical errors were propagated. The error of the majority of line intensities and self-broadening parameters is below 1%. The accuracy of most speed dependence parameters is better than 10%.

The parameters were compared to spectroscopic databases and independent experimental works. Intensities were also compared to *ab initio* calculations. The comparison of line intensities and self-broadening parameters to HITRAN12 values exhibited significant differences larger than 20% for many lines whereas a comparison for large intensities with experimental values by Ptashnik et al. [31] shows a good agreement with a systematic deviation of only 0.12% for intensities higher than 2×10^{-20} cm $molecule^{-1}$. A remarkably good agreement, mostly below 1% on average, with *ab initio* intensities by Tennyson's group at UCL [34] can be observed over several orders of magnitude. It turned out that there is a vibrational band dependent offset and scatter that is attributed to calculation issues since experiment does not distinguish between vibrational states.

The list of retrieved line parameters is given as a supplementary file to this publication. Note that reported non main isotopologue line intensities are to be considered as relative due to the lack of knowledge of isotopologue abundances in the measured sample gas.

Acknowledgements

The authors want to thank Jonathan Tennyson and Lorenzo Lodi for providing the *ab initio* line intensity list. This work has been performed within the framework of the DFG projects under contract numbers BI 834/5-1 and BI 834/5-2.

Appendix A. Supplementary material

Supplementary data associated with this article can be found in the online version at http://dx.doi.org/10.1016/j.jqsrt.2017.02.013.

References

[1] Network for the Detection of Atmospheric Composition Change (NDACC). ⟨www.ndacc.org⟩.
[2] Total Carbon Column Observing Network. ⟨www.tccon.caltech.edu⟩.
[3] Schneider M, Hase F. Improving spectroscopic line parameters by means of atmospheric spectra: theory and example for water vapor and solar absorption spectra. J Quant Spectrosc Radiat Transf 2009;110:1825–1838. http://dx.doi.org/10.1016/j.jqsrt.2009.04.011.
[4] Schneider M, Hase F, Blavier JF, Toon GC, Leblanc T. An empirical study on the importance of a speed-dependent Voigt line shape model for tropospheric water vapor profile remote sensing. J Quant Spectrosc Radiat Transf 2011;112:465–474. http://dx.doi.org/10.1016/j.jqsrt.2010.09.008.
[5] Schneider M, Toon GC, Blavier JF, Hase F, Leblanc T. H_2O and δD profiles remotely sensed from ground in different spectral infrared regions. Atmos Meas Tech 2010;3:1599–1613. http://dx.doi.org/10.5194/amt-3-1599-2010.
[6] Schneider M, Sepúlveda E, García O, Hase F, Blumenstock T. Remote sensing of water vapour profiles in the framework of the Total Carbon Column Observing Network (TCCON). Atmos Meas Tech 2010;3:1785–1795. http://dx.doi.org/10.5194/amt-3-1785-2010.
[7] Rothman LS, Gordon IE, Babikov Y, Barbe A, Benner DC, Bernath PF, Birk M, Bizzocchi L, Boudon V, Brown LR, Campargue A, Chance K, Cohen EA, Coudert LH, Devi VM, Drouin BJ, Fayt A, Flaud J-M, Gamache RR, Harrison JJ, Hartmann J-M, Hill C, Hodges JT, Jacquemart D, Jolly A, Lamouroux J, Le Roy RJ, Li G, Long DA, Lyulin OM, Mackie CJ, Massie ST, Mikhailenko SN, Müller HSP, Naumenko OV, Nikitin AV, Orphal J, Perevalov V, Perrin A, Polovtseva ER, Richard C, Smith MAH, Starikova E, Sung K, Tashkun SA, Tennyson J, Toon GC, Tyuterev V, Wagner G. The HITRAN2012 molecular spectroscopic database. J Quant Spectrosc Radiat Transf 2013;130:4–50. http://dx.doi.org/10.1016/j.jqsrt.2013.07.002.
[8] Timofeyev Y, Virolainen Y, Makarova M, Poberovsky A, Polyakov A, Ionov D, Osipov S, Imhasin H. Ground-based spectroscopic measurements of atmospheric gas composition near Saint Petersburg Russia. J Mol Spectros 2016;323:2–14. http://dx.doi.org/10.1016/j.jms.2015.12.007.
[9] Birk M, Wagner G. Voigt profile introduces optical depth dependent systematic errors – detected in high resolution laboratory spectra of water. J Quant Spectrosc Radiat Transf 2016;170:159–168. http://dx.doi.org/10.1016/j.jqsrt.2015.11.008.
[10] Rosenkranz PW. Shape of the 5 mm oxygen band in the atmosphere. IEEE Trans Antennas Propag 1975;AP-23:498–506. http://dx.doi.org/10.1109/TAP.1975.1141119.
[11] Coudert LH, Martin-Drumel M-A, Pirali O. Analysis of the high-resolution water spectrum up to the Second Triad and to J=30. J Mol Spectros 2014;303:36–41. http://dx.doi.org/10.1016/j.jms.2014.07.003.
[12] Birk M, Wagner G. Temperature-dependent air broadening of water in the 1250–1750 cm^{-1} range. J Quant Spectrosc Radiat Transf 2012;113:889–928. http://dx.doi.org/10.1016/j.jqsrt.2011.12.013.
[13] Wagner G, Birk M, Schreier F, Flaud J-M. Spectroscopic database for ozone in the fundamental spectral regions. J Geophys Res 2002;107:4626. http://dx.doi.org/10.1029/2001JD000818.
[14] Wagner G, Birk M. New infrared spectroscopic database for chlorine nitrate. J Quant Spectrosc Radiat Transf 2003;82:443–460. http://dx.doi.org/10.1016/S0022-4073(03)00169-9.

[15] Birk M, Wagner G. Experimental line strengths of the ClO fundamental. J GeoPhys Res Atmos 1997;102:19199–19206. http://dx.doi.org/10.1029/97JD01312.
[16] Flaud J-M, Birk M, Wagner G, Orphal J, Klee S, Lafferty W. The Far Infrared Spectrum of HOCl: line Positions and Intensities. J Mol Spectrosc 1998;191:362–367. http://dx.doi.org/10.1006/jmsp.1998.7653.
[17] Wetzel G, Oelhaf H, Kirner O, Ruhnke R, Friedl-Vallon F, Kleinert A, Maucher G, Fischer H, Birk M, Wagner G, Engel A. First remote sensing measurements of ClOOCl along with ClO and $ClONO_2$ in activated and deactivated Arctic vortex conditions using new ClOOCl IR absorption cross sections. Atmos Chem Phys 2010;10:931–945. http://dx.doi.org/10.5194/acp-10-931-2010.
[18] Loos J, Birk M, Wagner G. Pressure broadening, -shift, speed dependence and line mixing in the ν_3 rovibrational band of N_2O. J Quant Spectrosc Radiat Transf 2015;151:300–309. http://dx.doi.org/10.1016/j.jqsrt.2014.10.008.
[19] Maki AG, Wells JS NISTStandard Reference Database 118: Wavenumber Calibration Tables from Heterodyne Frequency Measurements. ⟨http://www.nist.gov/pml/data/wavenum/⟩.
[20] Hase F, Blumenstock T, Paton-Walsh C. Analysis of the Instrumental Line Shape of High- Resolution Fourier Transform IR Spectrometers with Gas Cell Measurements and New Retrieval Software. Appl Opt 1999;38:3417–3422. http://dx.doi.org/10.1364/AO.38.003417.
[21] Loos J, Birk M, Wagner G. New Multispectrum Fitting Software Used at DLR for Analysis of Laboratory Fourier-Transform Molecular Spectra. The 13th HITRAN Conference; 2014, http://dx.doi.org/10.5281/zenodo.11156.
[22] Ngo NH, Lisak D, Tran H, Hartmann J-M. An isolated line-shape model to go beyond the Voigt profile in spectroscopic databases and radiative transfer codes. J Quant Spectrosc Radiat Transf 2013;129:89–100. http://dx.doi.org/10.1016/j.jqsrt.2013.05.034.
[23] Ngo NH, Lisak D, Tran H, Hartmann J-M. Erratum to An isolated line-shape model to go beyond the Voigt profile in spectroscopic databases and radiative transfer codes. [J. Quant. Spectrosc. Radiat. Transf. 129 (2013)[89–100]. J Quant Spectrosc Radiat Transf 2014;134:105. http://dx.doi.org/10.1016/j.jqsrt.2013.10.016.
[24] Tran H, Ngo NH, Hartmann J-M. Efficient computation of some speed-dependent isolated line profiles. J Quant Spectrosc Radiat Transf 2013;129:199–203. http://dx.doi.org/10.1016/j.jqsrt.2013.06.015.
[25] Tran H, Ngo NH, Hartmann J-M. Erratum to Efficient computation of some speed dependent isolated line profiles. [J. Quant. Spectrosc. Radiat. Transfer 129 (2013)[199-203]. J Quant Spectrosc Radiat Transf 2014;134:104. http://dx.doi.org/10.1016/j.jqsrt.2013.10.015.
[26] Fischer J, Gamache RR, Goldman A, Rothman LS, Perrin A. Total internal partition sums for molecular species in the2000 edition of the HITRAN database. J Quant Spectrosc Radiat Transf 2003;82:401–412. http://dx.doi.org/10.1016/S0022-4073(03)00166-3.
[27] Rodgers CD. Characterization and error analysis of profiles retrieved from remote sounding measurements. J Geophys Res 1990;95:5587. http://dx.doi.org/10.1029/JD095iD05p05587.
[28] Toth RA Linelist of water vapor parameters from 500 to 8000 cm^{-1}. ⟨http://mark4sun.jpl.nasa.gov/h2o.html⟩.
[29] Jacquinet-Husson N, Armante R, Scott NA, Chédin A, Crépeau L, Boutammine C, Bouhdaoui A, Crevoisier C, Capelle V, Boonne C, Poulet-Crovisier N, Barbe A, Benner DC, Boudon V, Brown LR, Buldyreva J, Campargue A, Coudert LH, Devi VM, Down M, Drouin B, Fayt A, Fittschen C, Flaud J-M, Gamache RR, Harrison JJ, Hill C, Hodnebrog Ø, Hu S-M, Jacquemart D, Jolly A, Jiménez E, Lavrentieva N, Liu A-W, Lodi L, Lyulin O, Massie S, Mikhailenko SN, Müller H, Naumenko O, Nikitin A, Nielsen C, Orphal J, Perevalov V, Perrin A, Polovtseva ER, Predoi-Cross A, Rotger M, Ruth AA, Yu S, Sung K, Tashkun SA, Tennyson J, Tyuterev V, Vander Auwera J, Voronin B, Makie A. The2015 edition of the GEISA spectroscopic database. J Mol Spectros 2016;112:2395–2445. http://dx.doi.org/10.1016/j.jms.2016.06.007.
[30] Mikhailenko SN, Keppler Albert KA, Mellau G, Klee S, Winnewisser BP, Winnewisser M, Tyuterev V. Water vapor absorption line intensities in the 1900–6600 cm-1 region. J Quant Spectrosc Radiat Transf 2008;109:2687–2696. http://dx.doi.org/10.1016/j.jqsrt.2008.07.006.
[31] Ptashnik IV, McPheat R, Polyansky OL, Shine KP, Smith KM. Intensities and self-broadening coefficients of the strongest water vapour lines in the 2.7 and 6.25 μm absorption bands. J Quant Spectrosc Radiat Transf 2016;177:92–107. http://dx.doi.org/10.1016/j.jqsrt.2016.02.001.
[32] Pogány A, Klein A, Ebert V. Measurement of water vapor line strengths in the 1.4-2.7 μm range by tunable diode laser absorption spectroscopy. J Quant Spectrosc Radiat Transf 2015;165:108–122. http://dx.doi.org/10.1016/j.jqsrt.2015.06.023.
[33] Lodi L, Tennyson J, Polyanski OL. A global, high accuracy ab initio dipole moment surface for the electronic ground state of the water molecule. J Chem Phys 2011;135:034113. http://dx.doi.org/10.1063/1.3604934.
[34] Birk M, Wagner G, Loos J, Lodi L, Polyansky OL, Kyuberis AA, Zobov NF, Tennyson J. Accurate line intensities for water transitions in the infrared: comparison of theory and experiment. J Quant Spectrosc Radiat Transf 2017;203:88–102.
[35] Toth RA, Brown LR, Plymate C. Self-broadened widths and frequency shifts of water vapor lines between 590 and 2400 cm^{-1}. J Quant Spectrosc Radiat Transf 1998;59:529–562. http://dx.doi.org/10.1016/S0022-4073(97)00144-1.
[36] Toth RA. Measurements and analysis (using empirical functions for widths) of air- and self-broadening parameters of H_2O. J Quant Spectrosc Radiat Transf 2005;94:1–50. http://dx.doi.org/10.1016/j.jqsrt.2004.08.041.
[37] Mandin J-Y, Flaud J-M, Camy-Peyret C, Guelachvili G. Measurements and calculations of self-broadening coefficients of lines belonging to the ν_2 band of $H_2{}^{16}O$. J Quant Spectrosc Radiat Transf 1980;23:351–370. http://dx.doi.org/10.1016/0022-4073(80)90077-1.
[38] Mandin J-Y, Camy-Peyret C, Flaud J-M, Guelachvili G. Measurements and calculations of self-broadening coefficients of lines belonging to the $2\nu_2$, ν_1, and ν_3 bands of $H_2{}^{16}O$. Can J Phys 1982;60:94–101. http://dx.doi.org/10.1139/p82-013.
[39] Antony BK, Gamache RR. Self-broadened half-widths and self-induced line shifts for water vapor transitions in the 3.2–17.76 μm spectral region via complex Robert–Bonamy theory. J Mol Spectrosc 2007;243:113–123. http://dx.doi.org/10.1016/j.jms.2006.12.003.